Graphical Abstract

Predicting Plastic Events and Quantifying the Local Yield Surface in 3D Model Glasses

Dihui Ruan, Sylvain Patinet, Michael L. Falk

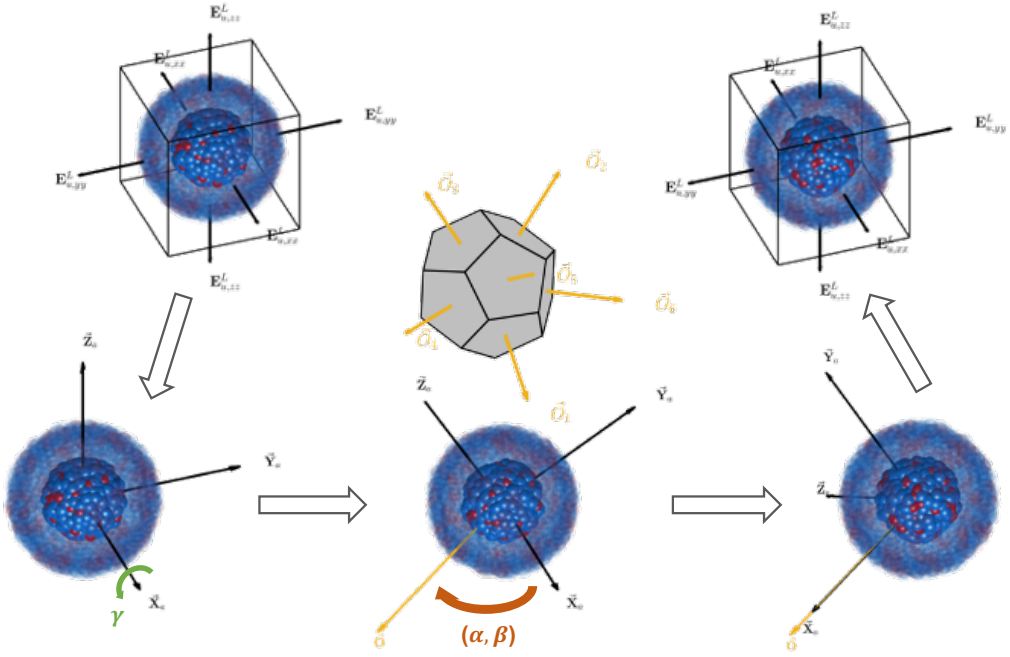

Highlights

Predicting Plastic Events and Quantifying the Local Yield Surface in 3D Model Glasses

Dihui Ruan, Sylvain Patinet, Michael L. Falk

- The local yield stress method is proven to be predictive to the plasticity in 3D glasses, and at the meanwhile, to be scalable to much larger samples compared to other computational predictors.
- The optimal probing region size of the local yield stress method is approached by optimization on the predictivity in plasticity as well as the extreme value distribution indicating the size of shear transformation zones.
- Quantifying The local yield surface in 3D opens up the window for studying the anisotropy of the local plasticity intriguing to the community of solid mechanics.

Predicting Plastic Events and Quantifying the Local Yield Surface in 3D Model Glasses

Dihui Ruan[a,], Sylvain Patinet[b], Michael L. Falk[a,c,d]

[a]*Department of Materials Science and Engineering, Johns Hopkins University, 3400 North Charles Street, Baltimore, 21093, Maryland, USA*
[b]*PMMH, CNRS, ESPCI Paris, Université PSL, Sorbonne Université, Université de Paris, 7 quai St Bernard, Paris, 75005, , France*
[c]*Department of Mechanical Engineering, and Department of Physics and Astronomy, Johns Hopkins University, 3400 North Charles Street, Baltimore, 21093, Maryland, USA*
[d]*Hopkins Extreme Materials Institute, Johns Hopkins University, 3400 North Charles Street, Baltimore, 21093, Maryland, USA*

Abstract

By applying the local yield stress (LYS) method to probe local regions of three-dimensional computational glass models, we confirm high correlations between the measured local yield stress ($\Delta\tau_c$) and the plastic events when the parameterization of the method is properly optimized. The optimal probing region for this system is found to be $\sim 5\sigma$ in radius, where σ represents the Lennard-Jones length scale, approximately the atomic size. The averaged correlation remains positive through the first 200 identified plastic events or 1/3 of the yielding strain ($\sim 7\%$). Here we apply only the local probing that aligns perfectly with the loading on the boundary. The LYS measurements converge to a Weibull distribution with a minimum $\Delta\tau_c$ indistinguishable from zero at larger probing region radii. Analysis of the data in light of an assumption that $\Delta\tau_c$ is a local quantity that obeys extreme value statistics above a critical length scale bounds the exponent of the underlying distribution of $\Delta\tau_c$ to lie between 1.26 and 1.71. A thorough investigation of the anisotropy of the local yield surface at the location of the first plastic event indicates that the first triggered region does not align perfectly with the loading on the boundary, but is well-predicted by projecting the shear applied at the boundary onto the local yield surface. This implies that the

*Authors have no competing interests, and MLF is the corresponding author.
Email address: mfalk@jhu.edu (Michael L. Falk)

correlation between the local yield stress prediction and the resulting plasticity may be enhanced by performing a more complete assessment of the local yield surface at each sample point.

Keywords: Plasticity, Local Yield Stress, Shear Transformation Zone, Amorphous Solids, Athermal Quasi-static Method
PACS: 0000, 1111
2000 MSC: 0000, 1111

1. Introduction

The detailed micro-mechanism of the mechanical response under an elastoplastic deformation in amorphous materials remains poorly characterized relative to their crystalline counterparts in which dislocations can be well specified.[1, 2, 3, 4]. Falk and Langer[5] postulated a shear transformation zone (STZ) model in which preexisting defects corresponding to local clusters of atoms/molecules rearrange cooperatively and irreversibly during plastic flow. This STZ concept has been incorporated into constitutive equations for describing elastoplastic behaviors [6, 7, 8, 9, 10, 11, 12, 13, 14] as well as into discrete models of amorphous plastic response[15, 16]. The existence of such defects in amorphous solids has been supported by experimental studies[17, 18, 19, 20] and atomic simulations[21, 22, 23, 24] in various types of glasses.

Researchers have been keenly interested in how one might accurately locate and characterize such 'flow-defects', and in doing so have measured the correlation of plastic events with a variety of proposed structurally derived predictors.[25] These predictors range from trivial structural parameters such as local density[26], atomic potential energy[22, 13], and short-range order[23, 27, 28], through more complex metrics obtained via machine learning[29, 30], quantification of local excitations induced by linear[31, 32, 33, 34] or nonlinear[35, 36] vibrational modes, by probing activation via the minimal energy path[37, 38], and by measurement of local elastic moduli[39, 40, 41]. Such simulations require a sample sufficiently large to resolve multiple individual STZs. Most of these investigations considered two-dimensional glasses consisting of $\sim 10,000$ atoms. Few analyses in three-dimensional glasses have been performed at comparable length scales, as this requires million-atom simulations prepared by quenching a liquid sufficiently slowly to produce a glass stable enough to compare with

experiments.[27, 28, 34, 29, 30]

In the context of the above indicators, Patinet *et al.* [42, 43] developed the local yield stress (LYS) method in which local regions are sheared at a particular length scale and loading orientation until yielding is triggered. By measuring the incremental stress to yield, the LYS method provides a direct measurement of elastoplastic response. High correlations have been observed between low local yield stresses and the sites where plastic events are observed during subsequent shear simulations of the material as a whole. A recent comparison found that this method ranks highly among a large number of structural indicators in 2D glassy samples, and performs best amongst these comparators in deeply quenched glasses, those modeled samples most comparable to as-quenched glasses produced in laboratory and industrial processes.[25] The LYS framework also quantifies atomistic data in ways that clearly relate to the yield surface, a continuum concept critical for understanding plasticity at the macro-scale [44, 45]. Characterizing larger 3D glasses has presented a challenge for diagonalization-based methods such as the identification of 'soft' spots in Reference [33]. Recent advances have provided more efficient ways to explore low-frequency modes to locate STZs, but comprehensive characterization of a material using such methods remains a challenge [46]. The computational expense for the LYS method scales with the system size as $\mathcal{O}(N)$ making it applicable to these larger three-dimensional systems.

Here we apply the LYS method to measure spatial variations in the incremental stress to yield ($\Delta\tau_c$) along a single local probing determined by a strain tensor. The resulting measurements of $\Delta\tau_c$ exhibit a correlation with the locations of the local plastic events produced by a similarly oriented strain applied at the boundary. The correlation persists until about 1/3 of the yielding strain when undertaken at the optimal length scale, $\sim 5\sigma$(atomic diameters) in radius.

Variation in the local probing strain is also examined at the location of the first identified plastic event. These data indicate that the triaxiality, orientation, rotation, and sign of the resulting plastic event aligns well with what one would infer from the measured local yield surface, but does not exactly correspond with the strain applied at the boundary. This suggests that the correlation of $\Delta\tau_c$ with the observed plastic events would improve if the entire local yield stress surface, rather than only the value of $\Delta\tau_c$ along the direction of the applied shear, were to be characterized throughout the material.

2. Sample Preparation

We perform molecular dynamics (MD) simulations to prepare three independent Kob-Andersen (KA)[47] binary Lennard-Jones (LJ) glasses within the Large-scale Atomic/Molecular Massively Parallel Simulator (LAMMPS) environment[48]. In each sample, 1,000,000 atoms are simulated in a cubic simulation box with periodic boundary conditions along the x, y and z axes. The system is comprised of 80% large atoms (A) and 20% small atoms (B). We apply a smoothed 6-12 Lennard-Jones(LJ) potential[49] field to quantify the interatomic interactions.

According to a prior study by Shi and Falk[24], shear bands only arise during deformation in KA glasses prepared with relatively low quenching rates. To focus on KA glasses susceptible to strain localization, we follow the same preparation procedure to melt and equilibrate the initial configuration at a reservoir temperature $T = 0.87\epsilon/k_B$ under an external pressure $P = 8.5\epsilon/\sigma^3$, and we then cool this melt to $T = 0.03\epsilon/k_B$ while releasing the pressure to $P = 0\epsilon/\sigma^3$ linearly over a duration of $2000t_0$ using a Nose-Hoover thermostat[50, 51] and Parrinello-Rahman barostat[52]. We verify that the difference in the potential energy per atom at the as-quenched state between our samples and the corresponding KA glasses in Reference [24] results from our choice of the smoothed LJ potential and the difference in the aspect ratio of the box dimension. Minimization of the energy via a conjugate gradient scheme[53] under zero pressure conditions is undertaken until achieving the convergence of the total force norm of the whole system. This is followed by a second force minimization with constrained volume for studying the athermal mechanical response at zero temperature. The final box dimension of these three KA glasses is approximately $93.4\sigma \times 93.4\sigma \times 93.4\sigma$, where x and y dimensions are comparable to those of the 2D systems previously studied by the local yield stress method[43, 42]. The configurations of all 3 glasses can be found on Johns Hopkins University Data Archive[54].

3. Three-Dimensional Local Yield Stresses

3.1. 3D Local Yield Stress Method

Patinet *et al.* developed the local yield stress (LYS) method in Reference [42] based upon the assumption that plastic events in amorphous solids occur as localized rearrangements located at STZs[5]. In the LYS method, local regions of atoms are sheared to the point of mechanical instability identified

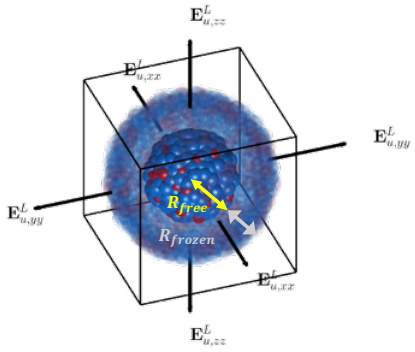

Figure 1: Schematics of a spherical region of atoms cut from the simulation box for local probing in a 3D binary glass with large (blue) and small (red) particles. The atoms in transparency form a shell of the core atoms shown in solid color. R_{free} and R_{frozen} are labeled by arrows in yellow and grey respectively. The black arrows denote the loading on the local boundary in Eq.6.

by a stress drop, and the incremental stress required to reach the yielding point is recorded as the local yield stress ($\Delta\tau_c$). A low value of $\Delta\tau_c$ indicates relative high susceptibility to plasticity. In our three-dimensional LYS analyses, spherical regions of atoms within a radius $R_{free} + R_{frozen}$ are probed by the athermal quasi-static (AQS) method[55, 56, 39, 57, 58, 59] within the Large-scale Atomic/Molecular Massively Parallel Simulator (LAMMPS) environment[48]. The atoms in the inner core with radius R_{free} are referred to as the 'free' atoms, and the atoms in the outer shell with thickness R_{frozen} are referred to as the 'frozen' atoms, as is shown in Figure 1. At each increment of loading, the 'frozen' atoms are deformed affinely with respect to the probing strain, and the 'free' atoms bounded by the 'frozen' shell undergo static relaxation into the nearest mechanically stable configuration using a conjugate gradient method[53]. R_{frozen} is set to be 5σ, twice the smoothed LJ potential cutoff radius $r_{out} = 2.5\sigma$, to include all relevant neighbor atoms for the 'free' atoms.

An increment of local loading $\Delta\boldsymbol{E}^L$ with a constant volume can be written in terms of a strain step magnitude Δe^L multiplied by a unit local strain tensor $\boldsymbol{E}^L_u$ as

$$\Delta\boldsymbol{E}^L = \Delta e^L \boldsymbol{E}^L_u. \tag{1}$$

The projected stress τ_p is defined as

$$\tau_p = \boldsymbol{S}^L : \boldsymbol{E}_u^L, \tag{2}$$

where $\boldsymbol{S}^L$ is the stress tensor of the local 'free' region. In the athermal limit[60, 61, 62, 63], the virial contribution of atom i can be computed as a tensor

$$\boldsymbol{\Phi}_i = \frac{1}{2} \sum_{j \neq i}^{N_p} \left(\vec{r}_{ij} \otimes \vec{f}_{ij} \right), \tag{3}$$

in which atom j is one of N_p atoms within the pairwise potential cutoff radius from atom i. The displacement vector $\vec{r}_{ij} = \vec{r}_j - \vec{r}_i$ represents the interatomic displacement, and $\vec{f}_{ij}$ represents the force exerted on atom i from atom j. $\boldsymbol{S}^L$ can then be estimated by dividing the sum of the virial contributions $\boldsymbol{\Phi}_i$ from the N_{free} atoms in the free region by its volume as

$$\boldsymbol{S}^L \approx \frac{3}{4\pi R_{free}^3} \sum_{i=1}^{N_{free}} \boldsymbol{\Phi}_i. \tag{4}$$

The projected stress τ_p is used to identify whether the response to an incremental strain is elastic or if, rather, an instability has been triggered. The stress tensor at the point when a stress drop is detected will be referred to as the onset stress $\boldsymbol{S}_{onset}^L$. This stress is used to calculate the local yield stress $\Delta\tau_c$ given by

$$\Delta\tau_c = (\boldsymbol{S}_{onset}^L - \boldsymbol{S}_0^L) : \boldsymbol{E}_u^L, \tag{5}$$

where $\boldsymbol{S}_0^L$ is the initial stress state of the local region before any probing. It is important to note that due to the residual stresses present in glasses, the elements in tensor $\boldsymbol{S_0}^L$ are typically not equal to zero. Since undertaking the local yield stress analysis in 3D is computationally demanding, we initially limit our investigation to the case where $\boldsymbol{E}_u^L$ is chosen to be a pure shear loading as

$$\boldsymbol{E}_u^L = \frac{\sqrt{2}}{2} \begin{bmatrix} 1 & 0 & 0 \\ 0 & -1 & 0 \\ 0 & 0 & 0 \end{bmatrix}. \tag{6}$$

To impose strain, equal tension and compression are applied along the x axis and the y axis while zero strain is imposed along the z axis, as illustrated in Figure 1. This plane strain boundary condition is comparable to the prior study on the 2D local yield stress method in Reference [42] and [43].

Table 1: Table of initial force tolerance F_{tol}^0, strain step Δe^L, and final force tolerance F_{tol} settings at each R_{free}. $*$: Δe^L (10^{-6}) is the smallest strain step achievable computationally given the available resources.

$R_{free}(\sigma)$	$F_{tol}^0(\epsilon/\sigma)$	Δe^L	$F_{tol}(\epsilon/\sigma)$
2.5	2×10^{-11}	10^{-4}	10^{-6}
3.75	3×10^{-11}	10^{-4}	10^{-6}
5	4×10^{-11}	10^{-5}	10^{-6}
7.5	8×10^{-11}	$10^{-6}*$	10^{-6}
10	2×10^{-10}	$10^{-6}*$	10^{-6}

3.2. Parameterization

The LYS method involves probing local regions with respect to a local unit strain tensor $\boldsymbol{E}_u^L$ and measuring the incremental stress required to induce a local instability. There are three parameters playing important roles in computing the local yield stress $\Delta\tau_c$: the force tolerance F_{tol} that sets the accuracy of force minimization when relaxing the 'free' atoms, the strain step Δe^L that controls the magnitude of each increment of loading, and the characteristic length R_{free} that determines the size of locally probed regions. The optimal values of these three parameters are not independent of each other. For instance, for larger R_{free} values, more atoms may participate in the plastic rearrangement, and the higher number of degrees of freedom necessitates a smaller strain step Δe^L.[58]

In Table 1, we list the parameters that are obtained from a series of convergence studies that we have undertaken to optimize the parameters. All the convergence studies are executed on sampling regions centered on evenly spaced $2 \times 2 \times 2$ grids extracted from the binary LJ glass samples described in **Materials and Methods**. For each listed R_{free} between 2.5σ and 10σ, an initial force tolerance F_{tol}^0 is chosen by sampling the convergence of the force norm when probing a very small strain 10^{-7}. Local yields stresses ($\Delta\tau_c$) are computed at various strain steps Δe^L, and these results are compared with the results using the smallest Δe^L (10^{-6}) we could achieve within our computational limitations. We choose the largest strain step Δe^L that results in a relative difference in $\Delta\tau_c \leqslant 1\%$ or we choose 10^{-6}, as noted in Table 1. With Δe^L set, we raise the values of F_{tol} to enhance the computational efficiency in the 3D LYS method. The final F_{tol} settings are determined by converging the computed $\Delta\tau_c$ with various F_{tol} values to be within $\leqslant 1\%$ of

the results using F^0_{tol}. We are able to raise the final F_{tol} values to 10^{-6} among all the R_{free} values without significantly affecting the results.

3.3. Distribution and Scaling

In order to uniformly sample the material response, local yield stresses ($\Delta\tau_c$) are computed in probing regions centered on evenly spaced grid points throughout the simulation box instead of probing regions centered on each atom as had been done in prior 2D studies[42]. The distance between grid points d_{sample} is chosen as $\sim 10\sigma$ to approach a set of $10 \times 10 \times 10$ samples in each Kob-Anderson (KA)[47] glass. From these samples, we are able to compute the distribution of $\Delta\tau_c$ in a representative manner. The distributions of local yield stress ($\Delta\tau_c$) with R_{free} from 2.5σ to 10σ are plotted in the inset of Figure 2(a). As was observed in the prior 2D studies[42, 43], increasing R_{free} results in more sampling regions yielding at lower $\Delta\tau_c$, and the peaks of these probability density functions (P_d) shift toward lower $\Delta\tau_c$ values with heavier low-end tails. This is consistent with our expectation that yielding behavior is controlled by the easiest to yield STZ in the sampling region. If we consider yield to be a local phenomenon, such that STZs are independent above a critical length scale (R^c_{free}), larger regions are expected to incorporate more STZs, and their $\Delta\tau_c$ should be lower on average than that of smaller regions that contain fewer STZs. If we assume that the observed yield stress is determined by the STZ with the lowest yield stress in the region, $\Delta\tau_c$ of a larger region is the minimum $\Delta\tau_c$ of all the included regions.

To test this assumption of 'isolated' local yield regions, we compare these distributions to the 'Extreme Value Distribution' (EVD)[64], which categorizes the distribution of maxima or minima of random variables. Since $\Delta\tau_c$ is defined to be non-negative, minima of sampled $\Delta\tau_c$ values are expected to result in a Weibull distribution when sampled at a length scale sufficiently larger than the scale on which distinct sub-regions would be independent.[65] For sufficiently large sampling regions, the probability density function (P_d) and cumulative distribution function (P_c) are therefore expected to be given by

$$P_d(\Delta\tau_c|a,b) = \frac{b}{a}\left(\frac{\Delta\tau_c}{a}\right)^{b-1} \exp\left[-\left(\frac{\Delta\tau_c}{a}\right)^{b}\right], \tag{7}$$

and

$$P_c(\Delta\tau_c|a,b) = 1 - \exp\left[-\left(\frac{\Delta\tau_c}{a}\right)^b\right], \tag{8}$$

where a is the scale parameter, and b is the shape parameter. As is presented in Figure 2(c), the scale parameter a is observed to decrease with increasing R_{free} corresponding to a lower mean when a larger local region is probed. Here, the shape parameter $b > 1$ indicates that the instantaneous 'yield rate'

$$M(\Delta\tau_c|a,b) = \frac{P_d(\Delta\tau_c)}{1 - P_c(\Delta\tau_c)} = \frac{b}{a}\left(\frac{\Delta\tau_c}{a}\right)^{b-1}, \tag{9}$$

the number of yield events per unit stress, increases with $\Delta\tau_c$.[66]

The fitted Weibull distributions are plotted as dot-dashed lines on top of the measured $\Delta\tau_c$ distributions in the main plot of Figure 2(a). Also, the corresponding cumulative distributions (P_c) of $\Delta\tau_c$ are presented in the inset of Figure 2(b). In the main plot of Figure 2(b), the cumulative distributions of $\Delta\tau_c$ are normalized by the two fitting parameters a and b in terms of $\ln\left[-\ln\left(1-P_c\right)\right]/b + \ln a$ and are then plotted versus $\ln\tau_y$ after being shifted by the corresponding mode. Combining the above plots, we notice that the distributions of $\Delta\tau_c$ align with the Weibull distribution for larger R_{free} values. More specifically, the density distribution functions in Figure 2(a) with $R_{free} = 7.5\sigma$ and 10σ are significantly Weibull-like. Therefore, the underlying distribution of $\Delta\tau_c$ at some critical length with R^c_{free} under 7.5σ is inferred to behave like a power-law distribution in the limit of $\Delta\tau_c \to 0$.[67]

Close inspection of the data taken with R_{free} from 2.5σ to 3.75σ, reveals that the lower-value tails in their probability density functions are heavier than what would be expected in an underlying distribution that would lead to a Weibull distribution. These distributions discontinuously drop to zero below a relatively high threshold, as shown in the main plot of Figure 2(a). We believe this indicates that lower $\Delta\tau_c$ values can't be accurately measured due to the limitations that the boundary constraints impose on local rearrangements within smaller regions. In comparison, the smooth $\Delta\tau_c$ distribution at $R_{free} = 5\sigma$ behaves like a power-law distribution as $\Delta\tau_c \to 0$. As we should expect, this distribution doesn't converge to a Weibull distribution since each probing region is too small to include a statistical number of independent STZs. We expect the characteristic length R^c_{free} of the underlying distribution is between 3.75σ and 5σ, and that 5σ is the closet to R^c_{free} among all the R_{free} values measured here. By this reasoning, we can

bound b^*, the exponent of the power law of the underlying $\Delta\tau_c$ distribution at R^c_{free} when $\Delta\tau_c \to 0$, to be greater than 1.26 as shown by the slope of the log-log distribution at the lower end when $R_{free} = 5\sigma$ in Figure 2(a). If we could measure larger and larger R_{free} values, the shape parameter b used to fit the Weibull distribution to the data in Figure 2(d) should converge to b^*.[67] Since the value of b^* is expected to be lower than the b from the fitted Weibull distribution with $R_{free} = 10\sigma$, we can bound b^* to be less than 1.71 according to Figure 2(d).

Based on the derivation of the extreme value statistics, the mean $\Delta\tau_c$ when probing larger regions whose size is far above the critical length R^c_{free} can be related to the cumulative distribution P^*_c in terms of N, the number of STZs in the probing region as[67]

$$< \Delta\tau_c >= P_c^{*-1}\left(\frac{1}{N+1}\right). \tag{10}$$

If we suppose R^c_{free} to be 5σ, $N(R_{free} = 7.5\sigma) \approx 11$ and $N(R_{free} = 10\sigma) \approx 47$ accordingly. While we intuitively expect that $N \propto R^3_{free}$, this is not consistent with the above two R_{free} values, indicating that we are not at sufficiently large R_{free} values to have fully converged to the Weibull distribution, or that the distribution at 5σ is not sufficiently close to the underlying distribution for this analysis to be viable.

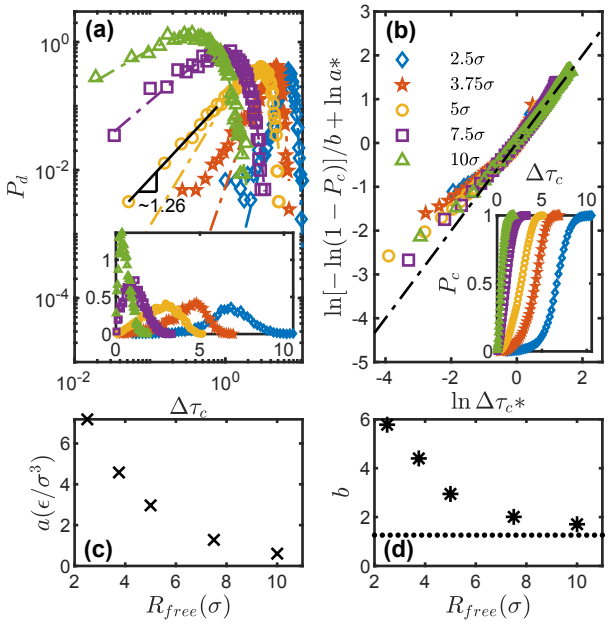

Figure 2: Local yield stress ($\Delta\tau_c$) distributions with R_{free}=2.5σ($\diamond$), 3.75σ($\star$), 5σ($\circ$), 7.5σ($\square$), and 10σ($\triangle$). (a) Log-log plot of $\Delta\tau_c$ probability density function (P_d). Dot-dashed lines denote Weibull distribution fits (Eq.7). The black solid line denotes the slope of the log-log distribution at $\Delta\tau_c \to 0$ with $R_{free} = 5\sigma$. Inset: linear-linear plot of the probability density function of $\Delta\tau_c$. (b) Scaled plot of the normalized cumulative distribution function of $\Delta\tau_c$, where the dot-dashed line denotes for a linear guideline extrapolated from $\Delta\tau_c$ distribution with $R_{free} = 10\sigma$. *: The curves are shifted by their corresponding modes. Inset: the cumulative distribution of $\Delta\tau_c$. Plot of (c) the scale parameter a ($\times$) and (d) the shape parameter b ($*$) from the Weibull distribution fits in Figure 2 versus R_{free}. The dotted line in (d) denotes the lower bound for b to converge with extremely large R_{free}. The original data in this figure can be found on Johns Hopkins University Data Archive[54].

4. Locating Plastic Events

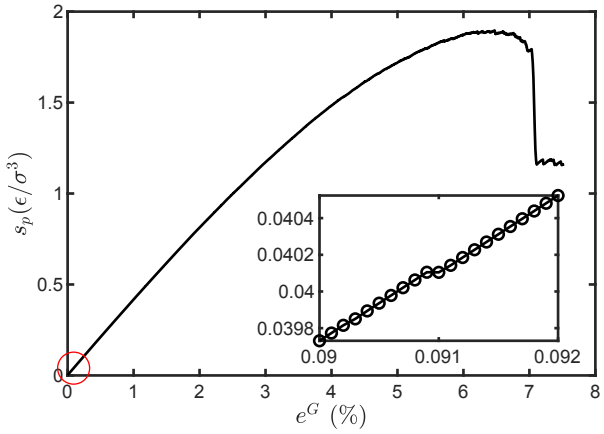

Figure 3: Stress-strain response for the AQS deformation with a strain step $\Delta e^G = 10^{-6}$ on one KA glass. The inset is the zoom-in view of the circled region in the main plot, where the first plastic event is identified. The original data of the stress-strain response for all 3 independent glasses can be found on Johns Hopkins University Data Archive[54].

To identify the series of plastic events that arise during loading, the simulation box is deformed via the AQS method within the LAMMPS environment. The AQS method affinely deforms the simulation box as all atoms are statically relaxed to a mechanically equilibrated state at each strain step. Here, the conjugate gradient method is deployed to minimize the forces during the relaxation. The load on the boundary is applied in the same manner as the locally-probed deformation described by Eq.6. At each strain step applied on the boundary (Δe^G), a projected stress for the simulation box (s_p) is recorded to characterize the stress-strain response,

$$s_p = \boldsymbol{S}^G : \boldsymbol{E}_u^G, \tag{11}$$

where $\boldsymbol{E}_u^G$ denotes the unit global strain tensor. The stress tensor of the system $\boldsymbol{S}^G = \frac{1}{V}\sum_{i=1}^{N} \boldsymbol{\Phi}_i$, where V is the volume of the simulation box and N is the total number of atoms in the system. A plastic event is identified by each instance in which the stress (i.e., s_p) decreases. These 3D KA glasses exhibit a discontinuous drop in the stress due to strain localization

at approximately 7% strain with strain step 10^{-6}, as is indicated in Figure 3. Due to the relatively large size of these 3D systems, many plastic events are triggered during deformation. This makes the serrations difficult to resolve by eye, in contrast to the obvious fluctuations in some previously studied 2D glasses[43]. The inset presents the first identified plastic event with a stress drop of $\sim 5.30 \times 10^{-7} \epsilon/\sigma^3$ and a triggering strain of $\sim 0.091\%$. As was noted in Reference [68], the identified plastic events depend on the strain step. This means that smaller and smaller plastic events are observed to occur at smaller and smaller strain as the strain step is decreased. Due to computational limitations, it is not possible to converge Δe^G to determine if there is a 'true' first plastic event in our prepared glasses with 1,000,000 atoms, and answering that question is not the objective of this work. Rather we assume that the strain step determines the resolution at which we are able to sample plastic rearrangements during deformation of the simulation box. We apply the loading on the boundary with the smallest strain step which is computationally affordable (10^{-7}) until the first stress drop in an effort to characterize the smallest length scale at which 3D Hooke's law behavior is recovered. For testing the predictivity of the LYS method, consecutive plastic events are sampled every 10^{-6} strain.

5. Deviation from Hooke's Law

In determining the the region size set by R_{free}, the local yield stress method assumes that Hooke's law is valid at this length scale. An evaluation of the consistency of local material response with Hooke's law should thus set a lower bound on R_{free} in computing the local yield stresses ($\Delta\tau_c$). Here, we adopt the methodology developed by Tsamados *et al.*[39] to estimate the deviation from linear elasticity at a given length scale. The whole simulation box is deformed in increments of 10^{-7} strain. The virial contribution at each atom (Eq.3) is computed both at the initial as-quenched state ($\mathbf{\Phi}^G_{i,0}$) and at the first onset of instability ($\mathbf{\Phi}^G_{i,y}$), defined as the configuration prior to the first stress drop (at $0.012 \pm 0.007\%$). Instead of applying a Gaussian windowing function as in Reference [39], we sum these local contributions from N_H atoms within the sampling radius R_H, to remain consistent with the uniform contributions from the 'free' atoms when computing the local

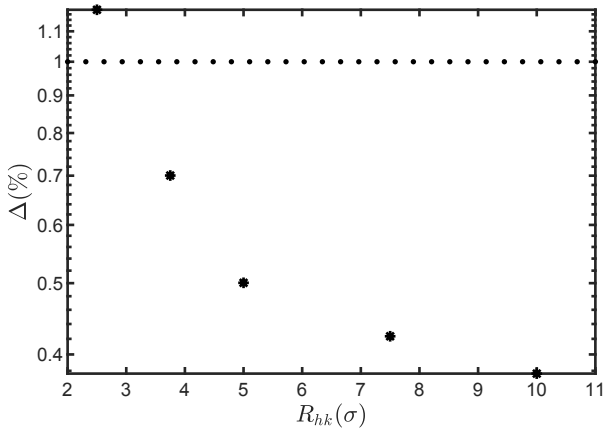

Figure 4: Log-linear plot of deviation from 3D Hooke's law versus averaging radius R_H. The standard errors are negligible compared with the size of the markers. The dotted line is the guideline for 1%.

yield stress ($\Delta\tau_c$). The stress change in this region is then approximated by

$$\boldsymbol{S}^G_{i,R_H} = \frac{3}{4\pi R_H^3} \sum_j^{N_H} \left(\boldsymbol{\Phi}^G_{j,y} - \boldsymbol{\Phi}^G_{j,0} \right). \tag{12}$$

By comparing the above two configurations, the atomic strain tensor centered at each atom is calculated with varying cutoff radii R_H according to References [5] and [69] using the OVITO open visualization tool[70]. A deformation gradient tensor $\boldsymbol{F}_i$ is computed by minimizing

$$\sum_{j=1}^{N_H} \left| \vec{r}_{ij,0} \boldsymbol{F}_i - \vec{r}_{ij,y} \right|^2, \tag{13}$$

where $\vec{r}_{ij,0}$ and $\vec{r}_{ij,y}$ are displacement vectors between atom j and i in the unstrained state and at the onset of instability respectively.[69] It follows that

$$\boldsymbol{F}_i = \left(\sum_{j=1}^{N_H} \vec{r}_{ij,0} \otimes \vec{r}_{ij,0} \right)^{-1} \left(\sum_{j=1}^{N_H} \vec{r}_{ij,0} \otimes \vec{r}_{ij,y} \right). \tag{14}$$

The resulting atomic strain tensor centered at atom i is then calculated as

$$\boldsymbol{E}^G_{i,R_H} = \frac{1}{2} \left(\boldsymbol{F}_i^T \boldsymbol{F}_i - \boldsymbol{I} \right). \tag{15}$$

Consider the generalized 3D Hooke's law in Voigt notation

$$\tilde{\boldsymbol{S}} = \tilde{\boldsymbol{C}}\tilde{\boldsymbol{E}} \tag{16}$$

where, for instance, s_{xx} in $\tilde{\boldsymbol{S}}$ and e_{xx} in $\tilde{\boldsymbol{E}}$ represent for the stress and strain components along x direction on the yz plane, and c_{ijkl} in $\tilde{\boldsymbol{C}}$ denotes one of the 21 nonzero elastic constants from a 4th order elastic-moduli tensor. To solve for these 21 unknowns in the stiffness matrix, 21 linear equations must be generated from 4 independent deformations. The resulting solution is, in general, overdetermined. We apply the least-squares method[71] to optimize the 21 elastic moduli numerically. Preset bounds on the solutions are applied with regards to the bulk stiffness matrix of the whole system computed from LAMMPS.

We then perform 11 independent deformations on the simulation box with the unit strain tensor

$$\boldsymbol{E}_u^G = \frac{\sqrt{2\psi^2 - 4\psi + 8}}{\psi^2 - 2\psi + 4} \begin{bmatrix} 1 & 0 & 0 \\ 0 & \frac{\psi}{2} - 1 & 0 \\ 0 & 0 & -\frac{\psi}{2} \end{bmatrix}, \tag{17}$$

in which triaxiality $\psi = 0, 0.1, 0.2, 0.3, ..., 1$. For an atom i, the deformations with ψ ranging from 0.1 to 1 overdetermine the elastic constants in Eq.16. The length scale dependence of the overdetermined elastic constants is assessed by varying R_H from 2.5 to 10σ. At $\psi = 0$, an estimated stress tensor $\tilde{\boldsymbol{S}}_{i,R_H}^{G'}$ (in Viogt notation) is calculated by substituting the solved stiffness matrix and the strain tensor into Eq.16. Then $\tilde{\boldsymbol{S}}_{i,R_H}^{G'}$ is compared with the directly computed stress tensor $\tilde{\boldsymbol{S}}_{i,R_H}^{G}$ (in Viogt notation) from LAMMPS and its deviation is quantified by the relative root mean square as

$$\Delta_{i,R_H} = \sqrt{\frac{\left\| \tilde{\boldsymbol{S}}_{i,R_H}^{G'} - \tilde{\boldsymbol{S}}_{i,R_H}^{G} \right\|^2}{6 \left\| \tilde{\boldsymbol{S}}_{i,R_H}^{G} \right\|^2}}. \tag{18}$$

In Figure 4, the mean deviation averaged among all the atoms are plotted against the averaging radius R_H. If we choose the threshold for elastic behavior to be $\leq 1\%$ as in Reference [39], then the 3D Hooke's law is valid at a length scale R_H above 2.5σ, which can thus serve as the lower limit of R_{free} for the local yield stress method in the 3D glasses.

6. Correlation between $\Delta\tau_c$ and Plastic Events

Next, we would like to assess the degree of correlation of the localized plasticity with the local yield stress, and in doing so determine an optimal length scale for R_{free}. We consider multiple plastic events obtained by shearing with strain steps $\Delta e^G = 10^{-6}$. Each plastic event is identified by a stress (s_p) drop, and the yield point is recorded as the last configuration prior to instability. Considering two consecutive events, the end of the former event also serves as the reference point of the subsequent event, which is identified as the last configuration prior to a stress (s_p) increase after a relaxation. We locate the triggered plastic rearrangement and characterize its nature by comparing the configuration after relaxation to the configuration at the yield point. These two configurations are denoted by subscripts e, for end, and y, for yield, respectively. At each atom, the deviation from affinity D^2_{min} is calculated as

$$D^2_{min,i} = \sum_{j=1}^{N_{cut}} \left| \vec{r}_{ij,y} \boldsymbol{F}_i - \vec{r}_{ij,e} \right|^2 , \tag{19}$$

where, we solve for $\boldsymbol{F}_i$ as described in Eq.14. N_{cut} is the number of neighbor atoms within a cutoff radius 2.5σ[5] to the center atom i. At the Nth plastic event, the local yield stress $\Delta\tau_c$ is computed centered at atom a_N with the maximum value of D^2_{min} in the as-quenched configuration, and then this $\Delta\tau_{c,a_N}$ is compared with the distribution of $\Delta\tau_c$ above. To be consistent with the prior studies in the 2D LYS method[43, 42], we quantify the correlation as

$$C_N = 1 - 2P_c \left(\Delta\tau_{c,a_N} \right) , \tag{20}$$

where P_c is the cumulative distribution function of $\Delta\tau_c$.

For the first 200 identified plastic events, the correlation averaged over every 20 plastic events in 3 independent KA glasses is plotted against the number of the plastic event in Figure 5(a). The corresponding total average with each R_{free} is presented in Figure 5(b). The local yield stress ($\Delta\tau_c$) computed for $R_{free} = 5\sigma$ exhibits the highest total averaged correlation with the plastic events. The mean correlation with $R_{free} = 5\sigma$ remains positive through $\sim 2.5\%$ strain, about 1/3 of the yielding strain. The correlation of the first plastic event is shown separately by the solid markers in Figure 5(a), and these correlations decay rapidly with the number of plastic events with larger R_{free} values. The predictivity of the local yield stress method in 3D appears reasonably good in this preliminary study in which we consider only

the local probing that perfectly aligns with the deformation imposed at the box boundary. This optimal $R_{free} \sim 5\sigma$ is consistent with the length scale of the prior study in the 2D LYS method[43, 42], but the corresponding volume is significantly more substantial with $600 \sim 700$ atoms in each probing region in 3D.

We note that there exist some negative correlations in Figure 5(a) and (b). As discussed in the previous 2D LYS studies[43], the LYS measurements using larger values of R_{free} fail to account for the secondary STZs because their signature is obscured by other nearby low yield-stress STZs. In other words, spatial resolution is lost by increasing local patch size. This leads to rapid decay in the correlation at higher strains. The fact that off-axis rearrangements were not probed is also expected to result in the over-estimation on the local yield stress ($\Delta\tau_c$).

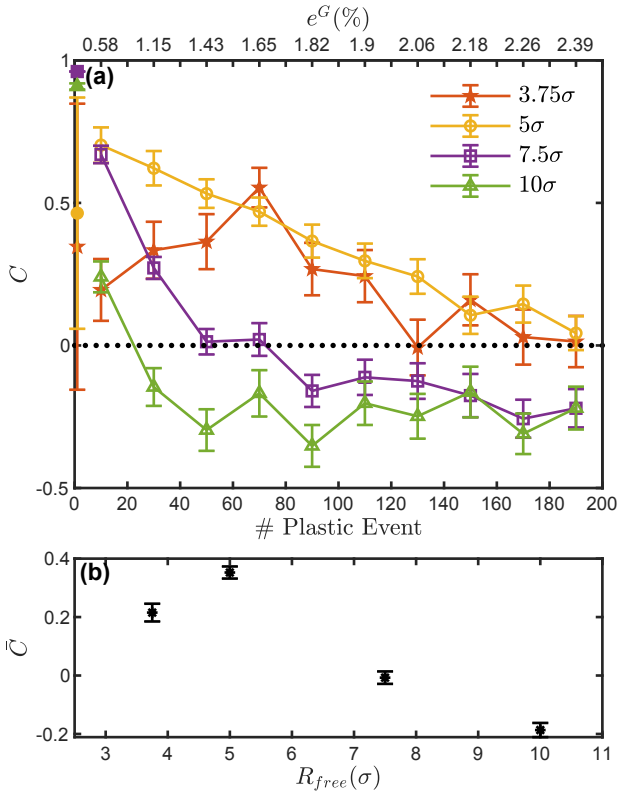

Figure 5: (a) Plot of correlation from Eq.20 versus the Nth plastic event with $3.75\sigma(\star)$, $5\sigma(\circ)$, $7.5\sigma(\square)$, and $10\sigma(\triangle)$. The hollow markers denote data points averaged over every 20 plastic events for 3 independent KA glasses. The 4 solid markers denote the mean correlation over the 3 glasses at the 1st plastic event. The standard errors are presented by the errorbars. The upper x-axis marks the corresponding triggering strain for each averaged correlation. The dotted line works as a guidance for $C = 0$. (b) Plot of the correlation averaged over all the plastic events in Subplot (a) versus R_{free}, with standard errors denoted by errorbars. The correlation with R_{free}=2.5σ is excluded due to its relatively large deviation from Hooke's law (see Figure 4).

7. Variation in Orientation, Rotation and Triaxiality

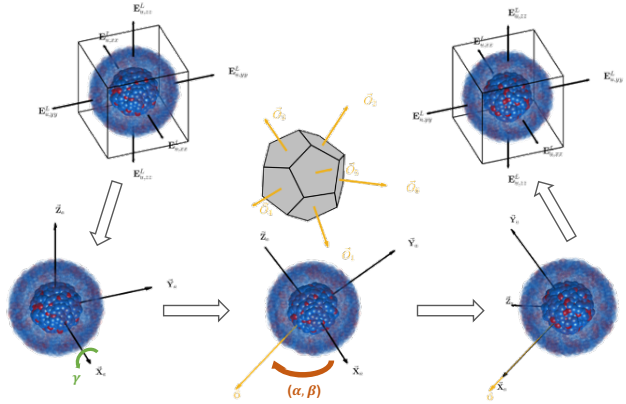

Figure 6: Schematics of rotating and probing a local region. The 'frozen' atoms in transparency form a shell of the core 'free' atoms shown in solid color. The black arrows on the local boundary denote the loading given by E_u^L in Eq.22 before (upper left) and after (upper right) the rotation. $(\vec{X}_a, \vec{Y}_a, \vec{Z}_a)$ represents for the coordinate system of the atoms rotating about $\vec{X}_a$ counter-clockwise with angle γ (green arrows) and then aligning $\vec{X}_a$ with a direction $\vec{O}$ (yellow arrows). $\vec{O}$ (yellow arrows) is sampled with respect to the face norms in a regular dodecahedron in the middle.

We expect that the local yield stress ($\Delta\tau_c$) is anisotropic in glasses. To explore this anisotropy, we vary the local probing and explore the $\Delta\tau_c$ yield surface in a representative and efficient way. For this purpose, we transform $\boldsymbol{E}_u^L$ to a rotated unit strain $\boldsymbol{E}_u^{L*}$ by applying the rotation matrix $\boldsymbol{R}\left(\vec{O}(\alpha,\beta),\gamma\right)$

$$\boldsymbol{E}_u^{L*} = \boldsymbol{R}^T\left(\vec{O}(\alpha,\beta),\gamma\right)\boldsymbol{E}_u^L\boldsymbol{R}\left(\vec{O}(\alpha,\beta),\gamma\right). \tag{21}$$

In order to maintain an orthogonal simulation box, we rotate the atoms in the local region such that the principal axes of $\boldsymbol{E}_u^L$ align with the basis vectors that define the simulation box, illustrated in Figure 6. $\boldsymbol{R}\left(\vec{O}(\alpha,\beta),\gamma\right)$ represents the general rotation tensor expressed as a function of $\vec{O}$, an arbitrary unit vector with which the x axis is brought into alignment, specified in terms of (α,β), a polar and an azimuthal angle respectively, and γ, an angle that describes a prior rotation about the x axis. To sample $\vec{O}$ evenly in 3D, we utilize the face norms of a regular dodecahedron. The resulting

rotation is illustrated in Figure 6. The atoms within the cut-out sphere are first rotated by an angle γ counterclockwise about $\vec{X}_a$ that is then rotated to align with a direction $\vec{O}$. After the rotation operation is applied on the atoms, a loading $\boldsymbol{E}_u^L$ is imposed on the local boundary. The deformation imposed on the principal axes may be expressed in terms of triaxiality ψ as

$$\boldsymbol{E}_u^L = \frac{\omega\sqrt{2\psi^2 - 4\psi + 8}}{\psi^2 - 2\psi + 4} \begin{bmatrix} 1 & 0 & 0 \\ 0 & \frac{\psi}{2} - 1 & 0 \\ 0 & 0 & -\frac{\psi}{2} \end{bmatrix}, \tag{22}$$

where, $\omega = -1$ (compression) or $+1$ (tension). ψ ranges from 0 to 1 inclusively, and in doing so determines the symmetry of the loading. If $\psi = 0$,

$$\boldsymbol{E}_u^L = \frac{\omega\sqrt{2}}{2} \begin{bmatrix} 1 & 0 & 0 \\ 0 & -1 & 0 \\ 0 & 0 & 0 \end{bmatrix}, \tag{23}$$

and a uniaxial loading strain is thus applied. With zero strain along z axis, this plane strain deformation recovers the local probing studied in the prior work regarding the two-dimensional LYS method[42, 43]. As ψ increases to 1,

$$\boldsymbol{E}_u^L = \frac{\omega\sqrt{6}}{2} \begin{bmatrix} 1 & 0 & 0 \\ 0 & -\frac{1}{2} & 0 \\ 0 & 0 & -\frac{1}{2} \end{bmatrix}, \tag{24}$$

resulting in a biaxial loading that is symmetric about the x axis.

For the sake of a preliminary study regarding the anisotropy of the local yield stress ($\Delta\tau_c$), we focus on the region centered around the single atom with the most dramatic plastic rearrangement as characterized by D^2_{min} from Eq.19 applied to the first plastic event identified in Figure 3 during the deformation of a 3D KA glass. When computing $\Delta\tau_c$, we choose $R_{free} = 5\sigma$ as the optimal length scale in the LYS method. Then we systematically vary the triaxiality ψ to take the values 0, 0.2, 0.4, 0.6, 0.8, and 1.0. At each ψ, we consider 6 orientation directions of $\vec{O}(\alpha, \beta)$ as shown in the middle of Figure 6. For each $\vec{O}(\alpha, \beta)$, the rotation angle γ is set to be 0°, 30°, 60°, 90°, 120°, and 150°.

In Figure 7, the calculated local yield stresses ($\Delta\tau_c$) are presented in a series of 2D plots with variation in rotation (γ), orientation ($\vec{O}$), triaxiality (ψ) and loading direction (ω). Each plot corresponds to a chosen set of ψ and $\vec{O}$, and the resulting $\Delta\tau_c$ from both compressive and tensile loadings is plotted for each value of γ. As expected, the projection must be a circle when $\psi = 1$ since $\boldsymbol{E}_u^L$ in Eq.24 is symmetric about the x axis. As ψ decreases to 0 (from right to left), $\Delta\tau_c$ loses this symmetry. The resulting $\Delta\tau_c$ projections from both loading directions ($\omega = -1, +1$) are consistent in their elongation, and it is generally the case that the compressive $\Delta\tau_c$ is slightly larger in magnitude than its corresponding tensile $\Delta\tau_c$, particularly for larger values of ψ.

In previous sections, the deformation on the box boundary given by $\boldsymbol{E}_u^G$ is identical to the shear of the local probing used to analyze the local value of $\Delta\tau_c$ given by $\boldsymbol{E}_u^L$. Here, we are able to cross-compare the propensity for the applied global loading to trigger the local yield stresses ($\Delta\tau_c$) measured along multiple probing directions, projecting each $\Delta\tau_c$ along the applied loading direction by calculating

$$f_p^2 = \boldsymbol{E}_u^{L*} : \boldsymbol{E}_u^G, \tag{25}$$

$$p_f = \frac{f_p^2}{|f_p^2|}\sqrt{|f_p^2|}, \tag{26}$$

such that the projected local yield stress is expressed as

$$\Delta\tau_y = \frac{\Delta\tau_c}{p_f}. \tag{27}$$

If $\boldsymbol{E}_u^{L*} = \boldsymbol{E}_u^G$, then $p_f = 1$ and the deformation on the box boundary aligns perfectly with the local probing when computing $\Delta\tau_c$. This is the case for our results in the previous sections. If $0 < p_f < 1$, the stress along $\boldsymbol{E}_u^G$ must be greater than $\Delta\tau_c$ itself in order to trigger the same local rearrangement probed by $\boldsymbol{E}_u^{L*}$. If $p_f < 0$, it indicates that the loading via $\boldsymbol{E}_u^G$ contributes in the opposite direction as that applied during the local probing $\boldsymbol{E}_u^{L*}$. This should indicate that it is impossible to trigger such a rearrangement by applying this $\boldsymbol{E}_u^G$.

The projected local yield stresses ($\Delta\tau_y$) along $\boldsymbol{E}_u^G$ in Eq.11 are mapped in Figure 8 with the same presentation as in Figure 7. Due to the fact that $\Delta\tau_y$ varies over a very large range, from -20ϵ/σ^3 to 20ϵ/σ^3 after being scaled by p_f in Eq.27, we only present the resultant $\Delta\tau_c$ with $\vec{O}_1$ corresponding to the

1st row in Figure 7, which are found to be generally lower in magnitude than those in other orientation directions. With all negative $\Delta\tau_y$ values neglected, all subplots are scaled to a radius of $5\epsilon/\sigma^3$. The minimum positive $\Delta\tau_y$ along all other $\vec{O}$ orientations is indicated by black dotted circles as a reference in each plot. The black crosses label the five smallest positive $\Delta\tau_y$ values. The $\Delta\tau_y$ locally probed with $\boldsymbol{E}_u^L$ in Eq.6 ranks as the 4th least in its value. This $\boldsymbol{E}_u^L$ aligns perfectly with $\boldsymbol{E}_u^G$ in the prior section, and the difference from the lowest $\Delta\tau_y$ is $\sim 8\%$ and is small in comparison to the highest level of the $\Delta\tau_y$ scale, $20\epsilon/\sigma^3$. This indicates that the easiest-to-trigger local rearrangement doesn't necessarily align with the loading imposed at the boundary, and the difference between the two appears to predominantly associated with the triaxiality ψ.

We are also curious to compare the triaxiality ψ of the corresponding local rearrangement centered at this targeted atom when applying $\boldsymbol{E}_u^G$ on the boundary. The atomic strain with averaging radius 5σ is computed according to Eq.15 by comparing the yielding configuration with the initial state. This strain tensor is an 'average' over the probing region, and this can be compared to the local probing presented by the effective unit strain tensor $\boldsymbol{E}_u^{L*}$ in Eq.21 after normalization. Accordingly, the eigenvalues of the normalized atomic strain tensor are then compared to $\boldsymbol{E}_u^L$ in Eq.22 and the resulting value of ψ is 0.465. This value falls between $\psi = 0.4$ and $\psi = 0.6$ which correspond to the 2nd and the 1st lowest $\Delta\tau_y$ marked in Figure 8. In addition, the p_f between the probing $\boldsymbol{E}_u^{L*}$ and the above averaged atomic strain yields ~ 0.938 for the minimal $\Delta\tau_y$ higher than $p_f \sim 0.896$ found for the $\Delta\tau_y$ when the local regions are probed aligning perfectly with the loading on the boundary (the 4th lowest). This high degree of correspondence indicates that the triggered local plastic event isn't necessarily in alignment with the loading on the boundary, but, rather the local arrangement could be well predicted by the minimum $\Delta\tau_y$ from the local yield surface. The correlation might be improved if a more complete range of local probing were undertaken at each sampling point, particularly with respect to the triaxiality ψ.

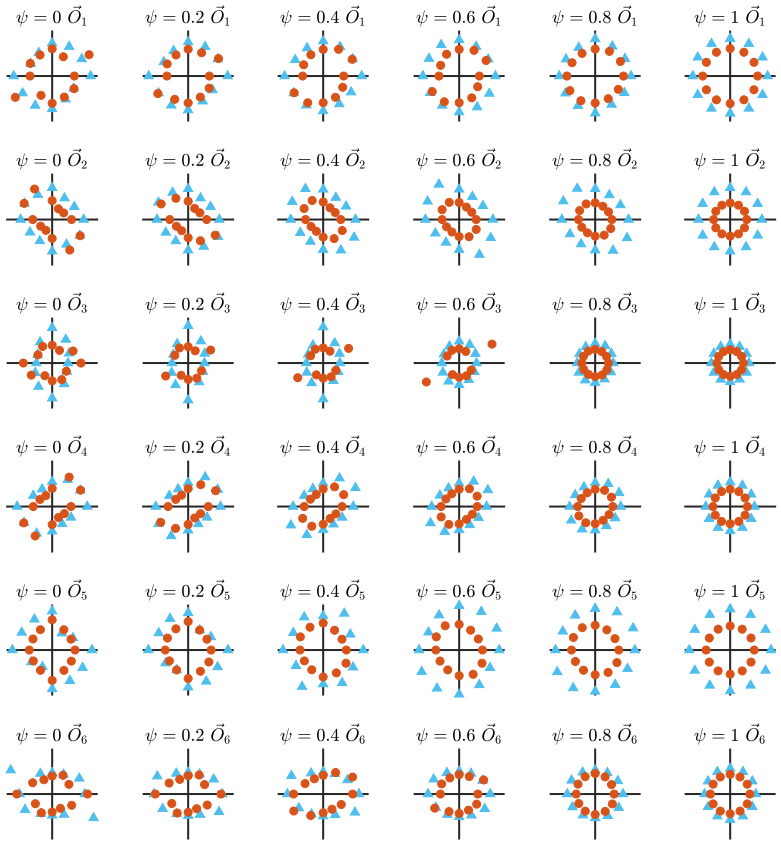

Figure 7: $\Delta\tau_c$ with variation in triaxiality ψ horizontally and orientation $\vec{O}$ vertically. In each subplot, rotation angle γ is plotted as the angle counterclockwise from the horizontal axis pointing to the right, and the magnitude of $\Delta\tau_c$ is represented by the distance from the origin. Blue $\triangle$ and red $\circ$ denote the results for $\omega = -1$ and $+1$ in Eq.22 respectively. All subplots are scaled with the limits of the axes as $5\epsilon/\sigma^3$. The original data can be found on Johns Hopkins University Data Archive[54].

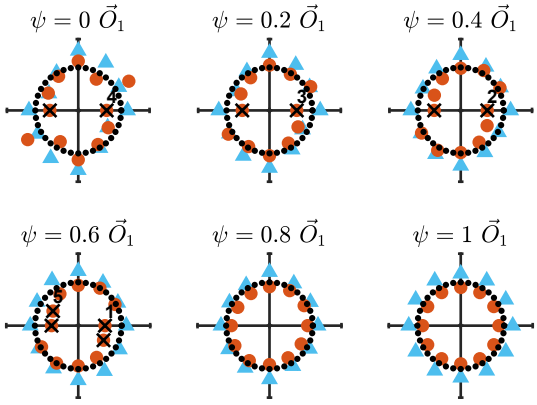

Figure 8: Projected local yield stress ($\Delta\tau_y$) calculated by Eq.25 to 27 with $\boldsymbol{E}_u^G$ in Eq.11. Only $\Delta\tau_y$ with $\vec{O}_1$ is plotted corresponding to the 1st row in Figure 7. Black crosses mark the five lowest values of $\Delta\tau_y$s with labeling 1 next to the smallest value. The black dotted circle labels the magnitude of the minimum $\Delta\tau_y$ among all other $\vec{O}$ orientations as a reference in each plot. All subplots are scaled with the limits of the axes as $5\epsilon/\sigma^3$. The original data can be found on Johns Hopkins University Data Archive[54].

8. Conclusions

By applying the local yield stress (LYS) method to a computational model of a three-dimensional glass and varying the local probing over a range of triaxialities (ψ), orientations ($\vec{O}(\alpha, \beta)$), rotations (γ), and directions (ω), we are able to obtain a sense of the complexity of the response of the glass microstructure when subjected to shear. We note that the optimal length scale for this analysis (approximately 5 atomic diameters in radius) is just above the smallest length scale at which the 3D Hooke's law remains valid, as was the case in 2D, although significantly more atoms reside within the resulting probing region (600-700 atoms) due to the higher dimensionality. When we are limited to probing at a shear identical to the loading on the boundary, the mean correlation after noise reduction persists through the first 200 identified plastic events or 1/3 the yielding strain ($\sim$ 7%). The local yield stress surface is significantly anisotropic. And the projected local yield stresses ($\Delta\tau_y$) with respect to the loading on the boundary does a very good job of predicting the sense of the shear at the first yield event. It is thus anticipated that the correlation of the yield stress analysis might be improved by characterizing the entire yield surface, rather than only the shear commensurate with that applied at the boundary, on each sampling point.

9. Acknowledgements

We would like to dedicate this work to Dr. Mark O. Robbins for his valuable advice and his mentorship over many, many years. Although Mark is no longer with us, his wisdom and passion towards scientific research will continue to inspire people who have known and communicated with him. We also would like to thank Dr. Bin Xu for sharing his experiences on the parameterization for the computational predictors and the presentations of multi-dimensional data. All the computations in this paper were performed at the Maryland Advanced Research Computing Center (MARCC). This project is supported by National Science Foundation(NSF) under Award No. DMR-1910066/1909733.

Appendix A. Sample Preparation

In each sample, 1,000,000 atoms are simulated in a cubic simulation box with periodic boundary conditions along the x, y and z axes. The system

is comprised of 80% large atoms (A) and 20% small atoms (B). We apply a smoothed 6-12 Lennard-Jones(LJ) potential to quantify the interatomic interactions as follows[43]:
When $r \leq r_{in}$,

$$U_{\alpha\beta}(r) = 4\epsilon_{\alpha\beta}\left[\left(\frac{\sigma_{\alpha\beta}}{r}\right)^{12} - \left(\frac{\sigma_{\alpha\beta}}{r}\right)^{6}\right] + C', \tag{A.1}$$

When $r_{in} < r \leq r_{out}$,

$$U_{\alpha\beta}(r) = C_0 + C_1(r - r_{in}) + C_2(r - r_{in})^2 + C_3(r - r_{in})^3 + C_4(r - r_{in})^4, \tag{A.2}$$

When $r > r_{out}$,

$$U_{\alpha\beta}(r) = 0, \tag{A.3}$$

with

$$C' = C_0 - 4\epsilon_{\alpha\beta}\left[\left(\frac{\sigma_{\alpha\beta}}{r_{in}}\right)^{12} - \left(\frac{\sigma_{\alpha\beta}}{r_{in}}\right)^{6}\right], \tag{A.4}$$

$$C_0 = -(r_{out} - r_{in})\left[3C_1 + C_2(r_{out} - r_{in})\right]/6, \tag{A.5}$$

$$C_1 = 24\epsilon_{\alpha\beta}\sigma^6_{\alpha\beta}(r^6_{in} - 2\sigma^6_{\alpha\beta})/r^{13}_{in}, \tag{A.6}$$

$$C_2 = 12\epsilon_{\alpha\beta}\sigma^6_{\alpha\beta}(26\sigma^6_{\alpha\beta} - 7r^6_{in})/r^{14}_{in}, \tag{A.7}$$

$$C_3 = -[3C_1 + 4C_2(r_{out} - r_{in})]/[3(r_{out} - r_{in})^2], \tag{A.8}$$

$$C_4 = [C_1 + C_2(r_{out} - r_{in})]/[2(r_{out} - r_{in})^3]. \tag{A.9}$$

α and β denote particle species A or B. In LJ units, all quantities are represented in terms of particle mass m, which is equivalent for both species, interatomic distance σ, and interaction energy ϵ. Consequently, time is measured in units of $t_0 = \sigma\sqrt{m/\epsilon}$, temperature in units of ϵ/k_B, pressure and stress in units of ϵ/σ^3, etc. In the Kob-Aderson[47] model, the bonding energies are $\epsilon_{AA} = 1.0\epsilon$, $\epsilon_{BB} = 0.5\epsilon$, $\epsilon_{AB} = \epsilon_{BA} = 1.5\epsilon$, and the equilibrium particle spacings are $\sigma_{AA} = 1.0\sigma$, $\sigma_{AA} = 0.88\sigma$, $\sigma_{AB} = \sigma_{BA} = 0.8\sigma$.[24] This potential field is smoothed from $r_{in} = 2.0\sigma$ to $r_{out} = 2.5\sigma$ via a polynomial function with coefficients C_0,C_1, C_2, C_3 and C_4 as shown in Eq.A.2, to avoid any discontinuity in the force associated with the potential's short-ranged cutoff.

Appendix B. Deviation from Hooke's Law

Appendix B.1. Elastic Constants for the Bulk Glasses

To estimate the bulk elastic constants, the simulation box is loaded independently along xx, yy, zz, or sheared along xy, xz, yz up to 1×10^{-7} strain using the athemal quasi-static (AQS) method [55, 56, 39, 57, 58, 59]. After strain is applied along each of the six probing directions, the elastic constants are calculated such that

$$c_{AB} = s_A / e_B \tag{B.1}$$

with A and B taking the values xx, yy, zz, xy, xz, or yz. For each loading, both positive and negative strain are applied and averaged. The $c_{AB} = c_{BA}$ elements are symmetrized as $(c_{AB} + c_{BA})/2$ for the off-diagonal elastic constants.

Appendix C. Variation in Orientation, Rotation and Triaxiality

The Projected Local Yield Stress $\Delta\tau_y$

The patterns of the Projected Local Yield Stress $\Delta\tau_y$ are presented in Fig. C.9. In the array of plots, triaxiality (ψ) is varied horizontally and orientation ($\vec{O}$) is varied vertically. In each plot, rotation angle (γ) is the angle counterclockwise from the horizontal axis pointing to the right, and the magnitude of $\Delta\tau_c$ is represented by the distance from the origin. Blue $\triangle$ and red $\circ$ denote the results for $\omega = -1$ and $+1$. Black crosses mark the five lowest values of $\Delta\tau_y$ where the label 1 indicates the smallest value. In addition, solid and hollow markers denote positive and negative sign respectively. In order to show the full range of values, each plot is scaled with the limits of the axes varied to ± 5, ± 10, ± 15, and $\pm 20\epsilon/\sigma^3$, and this variation in scaling is denoted by the yellow, light green, green, and dark green backgrounds, as is shown in the bottom subplot.

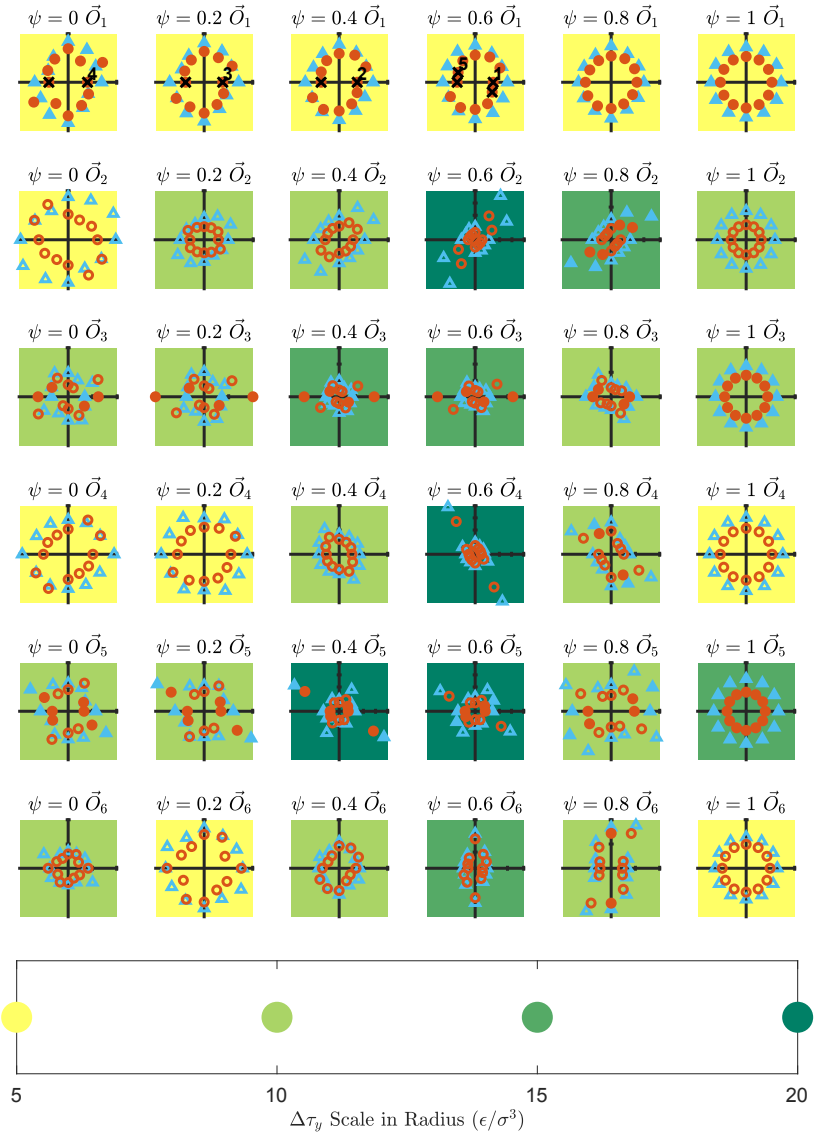

Figure C.9: Projected local yield stress ($\Delta\tau_y$).

References

[1] A. Stukowski, K. Albe, Extracting dislocations and non-dislocation crystal defects from atomistic simulation data, Modelling and Simulation in Materials Science and Engineering 18 (8) (2010) 085001. doi:10.1088/0965-0393/18/8/085001.

[2] W. Shockley, W. T. Read, Quantitative Predictions from Dislocation Models of Crystal Grain Boundaries, Physical Review 75 (4) (1949) 692–692. doi:10.1103/PhysRev.75.692.

[3] R. LeSar, Simulations of Dislocation Structure and Response, Annual Review of Condensed Matter Physics 5 (1) (2014) 375–407. doi:10.1146/annurev-conmatphys-031113-133858.

[4] W. Püschl, Models for dislocation cross-slip in close-packed crystal structures: A critical review, Progress in Materials Science 47 (4) (2002) 415–461. doi:10.1016/S0079-6425(01)00003-2.

[5] M. L. Falk, J. S. Langer, Dynamics of viscoplastic deformation in amorphous solids, Physical Review E 57 (6) (1998) 7192–7205. doi:10.1103/PhysRevE.57.7192.

[6] E. Bouchbinder, J. S. Langer, I. Procaccia, Athermal shear-transformation-zone theory of amorphous plastic deformation. II. Analysis of simulated amorphous silicon, Physical Review E 75 (3) (2007) 036108. doi:10.1103/PhysRevE.75.036108.

[7] E. Bouchbinder, J. S. Langer, I. Procaccia, Athermal shear-transformation-zone theory of amorphous plastic deformation. I. Basic principles, Physical Review E 75 (3) (2007) 036107. doi:10.1103/PhysRevE.75.036107.

[8] M. L. Manning, J. S. Langer, J. M. Carlson, Strain localization in a shear transformation zone model for amorphous solids, Physical Review E 76 (5) (2007) 056106. doi:10.1103/PhysRevE.76.056106.

[9] E. Bouchbinder, J. S. Langer, Nonequilibrium thermodynamics of driven amorphous materials. I. Internal degrees of freedom and volume deformation, Physical Review E 80 (3) (2009) 031131. doi:10.1103/PhysRevE.80.031131.

[10] E. Bouchbinder, J. S. Langer, Nonequilibrium thermodynamics of driven amorphous materials. II. Effective-temperature theory, Physical Review E 80 (3) (2009) 031132. doi:10.1103/PhysRevE.80.031132.

[11] E. Bouchbinder, J. S. Langer, Nonequilibrium thermodynamics of driven amorphous materials. III. Shear-transformation-zone plasticity, Physical Review E 80 (3) (2009) 031133. doi:10.1103/PhysRevE.80.031133.

[12] C. H. Rycroft, Y. Sui, E. Bouchbinder, An Eulerian projection method for quasi-static elastoplasticity, Journal of Computational Physics 300 (2015) 136–166. arXiv:1409.2173, doi:10.1016/j.jcp.2015.06.046.

[13] A. R. Hinkle, C. H. Rycroft, M. D. Shields, M. L. Falk, Coarse graining atomistic simulations of plastically deforming amorphous solids, Physical Review E 95 (5) (2017) 053001. doi:10.1103/PhysRevE.95.053001.

[14] K. Kontolati, D. Alix-Williams, N. M. Boffi, M. L. Falk, C. H. Rycroft, M. D. Shields, Manifold learning for coarse-graining atomistic simulations: Application to amorphous solids, arXiv:2103.00779 [physics] x (2021) x. arXiv:2103.00779.

[15] E. R. Homer, C. A. Schuh, Mesoscale modeling of amorphous metals by shear transformation zone dynamics, Acta Materialia 57 (9) (2009) 2823–2833. doi:10.1016/j.actamat.2009.02.035.

[16] M. Talamali, V. Petäjä, D. Vandembroucq, S. Roux, Strain localization and anisotropic correlations in a mesoscopic model of amorphous plasticity, Comptes Rendus Mécanique 340 (4) (2012) 275–288. doi:10.1016/j.crme.2012.02.010.

[17] F. Jiang, M. Q. Jiang, H. F. Wang, Y. L. Zhao, L. He, J. Sun, Shear transformation zone volume determining ductile–brittle transition of bulk metallic glasses, Acta Materialia 59 (5) (2011) 2057–2068. doi:10.1016/j.actamat.2010.12.006.

[18] Y. Ma, J. H. Ye, G. J. Peng, D. H. Wen, T. H. Zhang, Loading rate effect on the creep behavior of metallic glassy films and its correlation with the shear transformation zone, Materials Science and Engineering: A 622 (2015) 76–81. doi:10.1016/j.msea.2014.11.022.

[19] Y. Ma, J. H. Ye, G. J. Peng, D. H. Wen, T. H. Zhang, Nanoindentation study of size effect on shear transformation zone size in a Ni–Nb metallic glass, Materials Science and Engineering: A 627 (2015) 153–160. doi:10.1016/j.msea.2015.01.001.

[20] D. Pan, Y. Yokoyama, T. Fujita, Y. H. Liu, S. Kohara, A. Inoue, M. W. Chen, Correlation between structural relaxation and shear transformation zone volume of a bulk metallic glass, Applied Physics Letters 95 (14) (2009) 141909. doi:10.1063/1.3246151.

[21] N. V. Priezjev, Collective nonaffine displacements in amorphous materials during large-amplitude oscillatory shear, Physical Review E 95 (2) (2017) 023002. doi:10.1103/PhysRevE.95.023002.

[22] Y. Shi, M. B. Katz, H. Li, M. L. Falk, Evaluation of the Disorder Temperature and Free-Volume Formalisms via Simulations of Shear Banding in Amorphous Solids, Physical Review Letters 98 (18) (2007) 185505. doi:10.1103/PhysRevLett.98.185505.

[23] Y. Shi, M. L. Falk, Strain Localization and Percolation of Stable Structure in Amorphous Solids, Physical Review Letters 95 (9) (2005) 095502. doi:10.1103/PhysRevLett.95.095502.

[24] Y. Shi, M. L. Falk, Atomic-scale simulations of strain localization in three-dimensional model amorphous solids, Physical Review B 73 (21) (2006) 214201. doi:10.1103/PhysRevB.73.214201.

[25] D. Richard, M. Ozawa, S. Patinet, E. Stanifer, B. Shang, S. A. Ridout, B. Xu, G. Zhang, P. K. Morse, J.-L. Barrat, L. Berthier, M. L. Falk, P. Guan, A. J. Liu, K. Martens, S. Sastry, D. Vandembroucq, E. Lerner, M. L. Manning, Predicting plasticity in disordered solids from structural indicators, Physical Review Materials 4 (11) (2020) 113609. doi:10.1103/PhysRevMaterials.4.113609.

[26] F. Spaepen, A microscopic mechanism for steady state inhomogeneous flow in metallic glasses, Acta Metallurgica 25 (4) (1977) 407–415. doi:10.1016/0001-6160(77)90232-2.

[27] Y. Shi, M. L. Falk, Stress-induced structural transformation and shear banding during simulated nanoindentation of a metallic glass, Acta Materialia 55 (13) (2007) 4317–4324. doi:10.1016/j.actamat.2007.03.029.

[28] J. Ding, Y.-Q. Cheng, E. Ma, Full icosahedra dominate local order in Cu64Zr34 metallic glass and supercooled liquid, Acta Materialia 69 (2014) 343–354. doi:10.1016/j.actamat.2014.02.005.

[29] E. D. Cubuk, S. S. Schoenholz, J. M. Rieser, B. D. Malone, J. Rottler, D. J. Durian, E. Kaxiras, A. J. Liu, Identifying Structural Flow Defects in Disordered Solids Using Machine-Learning Methods, Physical Review Letters 114 (10) (2015) 108001. doi:10.1103/PhysRevLett.114.108001.

[30] S. S. Schoenholz, E. D. Cubuk, D. M. Sussman, E. Kaxiras, A. J. Liu, A structural approach to relaxation in glassy liquids, Nature Physics 12 (5) (2016) 469–471. doi:10.1038/nphys3644.

[31] A. Widmer-Cooper, H. Perry, P. Harrowell, D. R. Reichman, Irreversible reorganization in a supercooled liquid originates from localized soft modes, Nature Physics 4 (9) (2008) 711–715. doi:10.1038/nphys1025.

[32] A. Tanguy, B. Mantisi, M. Tsamados, Vibrational modes as a predictor for plasticity in a model glass, EPL (Europhysics Letters) 90 (1) (2010) 16004. doi:10.1209/0295-5075/90/16004.

[33] M. L. Manning, A. J. Liu, Vibrational Modes Identify Soft Spots in a Sheared Disordered Packing, Physical Review Letters 107 (10) (2011) 108302. doi:10.1103/PhysRevLett.107.108302.

[34] J. Ding, S. Patinet, M. L. Falk, Y. Cheng, E. Ma, Soft spots and their structural signature in a metallic glass, Proceedings of the National Academy of Sciences 111 (39) (2014) 14052–14056. doi:10.1073/pnas.1412095111.

[35] L. Gartner, E. Lerner, Nonlinear plastic modes in disordered solids, Physical Review E 93 (1) (2016) 011001. doi:10.1103/PhysRevE.93.011001.

[36] B. Xu, M. L. Falk, S. Patinet, P. Guan, Atomic nonaffinity as a predictor of plasticity in amorphous solids, Physical Review Materials 5 (2) (2021) 025603. doi:10.1103/PhysRevMaterials.5.025603.

[37] B. Xu, M. Falk, J. Li, L. Kong, Strain-dependent activation energy of shear transformation in metallic glasses, Physical Review B 95 (14) (2017) 144201. doi:10.1103/PhysRevB.95.144201.

[38] B. Xu, M. L. Falk, J. F. Li, L. T. Kong, Predicting Shear Transformation Events in Metallic Glasses, Physical Review Letters 120 (12) (2018) 125503. doi:10.1103/PhysRevLett.120.125503.

[39] M. Tsamados, A. Tanguy, C. Goldenberg, J.-L. Barrat, Local elasticity map and plasticity in a model Lennard-Jones glass, Physical Review E 80 (2) (2009) 026112. doi:10.1103/PhysRevE.80.026112.

[40] H. Mizuno, S. Mossa, J.-L. Barrat, Measuring Spatial Distribution of Local Elastic Modulus in Glasses, Physical review. E 87 (2013) 042306. doi:10.1103/PhysRevE.87.042306.

[41] B. Shang, J. Rottler, P. Guan, J.-L. Barrat, Local versus Global Stretched Mechanical Response in a Supercooled Liquid near the Glass Transition, Physical Review Letters 122 (10) (2019) 105501. doi:10.1103/PhysRevLett.122.105501.

[42] S. Patinet, D. Vandembroucq, M. L. Falk, Connecting Local Yield Stresses with Plastic Activity in Amorphous Solids, Physical Review Letters 117 (4) (2016) 045501. doi:10.1103/PhysRevLett.117.045501.

[43] A. Barbot, M. Lerbinger, A. Hernandez-Garcia, R. García-García, M. L. Falk, D. Vandembroucq, S. Patinet, Local yield stress statistics in model amorphous solids, Physical Review E 97 (3) (2018) 033001. doi:10.1103/PhysRevE.97.033001.

[44] A. C. Lund, C. A. Schuh, Yield surface of a simulated metallic glass, Acta Materialia 51 (18) (2003) 5399–5411.

[45] C. A. Schuh, A. C. Lund, Atomistic basis for the plastic yield criterion of metallic glass, Nature materials 2 (7) (2003) 449–452.

[46] D. Richard, G. Kapteijns, J. A. Giannini, M. L. Manning, E. Lerner, Simple and broadly applicable definition of shear transformation zones, Physical Review Letters 126 (1) (2021) 015501.

[47] W. Kob, H. C. Andersen, Testing mode-coupling theory for a supercooled binary Lennard-Jones mixture I: The van Hove correlation function, Physical Review E 51 (5) (1995) 4626–4641. doi:10.1103/PhysRevE.51.4626.

[48] LAMMPS: Large-scale Atomic/Molecular Massively Parallel Simulator, http://lammps.sandia.gov, LAMMPS: Large-scale Atomic/Molecular Massively Parallel Simulator, http://lammps.sandia.gov.

[49] J. E. Jones, S. Chapman, On the determination of molecular fields. —II. From the equation of state of a gas, Proceedings of the Royal Society of London. Series A, Containing Papers of a Mathematical and Physical Character 106 (738) (1924) 463–477. doi:10.1098/rspa.1924.0082.

[50] S. Nosé, A unified formulation of the constant temperature molecular dynamics methods, The Journal of Chemical Physics 81 (1) (1984) 511–519. doi:10.1063/1.447334.

[51] W. G. Hoover, Canonical dynamics: Equilibrium phase-space distributions, Physical Review A 31 (3) (1985) 1695–1697. doi:10.1103/PhysRevA.31.1695.

[52] M. Parrinello, A. Rahman, Polymorphic transitions in single crystals: A new molecular dynamics method, Journal of Applied Physics 52 (12) (1981) 7182–7190. doi:10.1063/1.328693.

[53] E. Polak, G. Ribiere, Note sur la convergence de méthodes de directions conjuguées, Revue française d'informatique et de recherche opérationnelle. Série rouge 3 (16) (1969) 35–43. doi:10.1051/m2an/196903R100351.

[54] D. Ruan, S. Patinet, M. L. Falk, Data associated with the publication: Predicting plastic events and quantifying the local yield surface in 3d model glasses, `https://doi.org/10.7281/T1/HVRF8B` (2021). doi:10.7281/T1/HVRF8B.

[55] A. Tanguy, F. Leonforte, J.-L. Barrat, Plastic response of a 2D Lennard-Jones amorphous solid: Detailed analysis of the local rearrangements at very slow strain rate, The European Physical Journal E 20 (3) (2006) 355–364. doi:10.1140/epje/i2006-10024-2.

[56] E. Lerner, I. Procaccia, Locality and nonlocality in elastoplastic responses of amorphous solids, Physical Review E 79 (6) (2009) 066109. doi:10.1103/PhysRevE.79.066109.

[57] R. Dasgupta, S. Karmakar, I. Procaccia, Universality of the Plastic Instability in Strained Amorphous Solids, Physical Review Letters 108 (7) (2012) 075701. doi:10.1103/PhysRevLett.108.075701.

[58] S. Karmakar, E. Lerner, I. Procaccia, Statistical physics of the yielding transition in amorphous solids, Physical Review E 82 (055103(R)) (Nov. 2010). doi:10.1103/PhysRevE.82.055103.

[59] C. Maloney, A. Lemaître, Universal Breakdown of Elasticity at the Onset of Material Failure, Physical Review Letters 93 (19) (2004) 195501. doi:10.1103/PhysRevLett.93.195501.

[60] D. M. Heyes, Pressure tensor of partial-charge and point-dipole lattices with bulk and surface geometries, Physical Review B 49 (2) (1994) 755–764. doi:10.1103/PhysRevB.49.755.

[61] T. W. Sirk, S. Moore, E. F. Brown, Characteristics of thermal conductivity in classical water models, The Journal of Chemical Physics 138 (6) (2013) 064505. doi:10.1063/1.4789961.

[62] A. P. Thompson, S. J. Plimpton, W. Mattson, General formulation of pressure and stress tensor for arbitrary many-body interaction potentials under periodic boundary conditions, The Journal of Chemical Physics 131 (15) (2009) 154107. doi:10.1063/1.3245303.

[63] D. Surblys, H. Matsubara, G. Kikugawa, T. Ohara, Application of atomic stress to compute heat flux via molecular dynamics for systems with many-body interactions, Physical Review E 99 (5) (2019) 051301. doi:10.1103/PhysRevE.99.051301.

[64] E. J. Gumbel, Statistics of Extremes, Dover Publications, Mineola, N.Y., 2004.

[65] W. Weibull, S. Stockholm, A Statistical Distribution Function of Wide Applicability, Journal of Applied Mechanics 18 (1951) 293–297.

[66] R. Jiang, D. N. P. Murthy, A study of Weibull shape parameter: Properties and significance, Reliability Engineering & System Safety 96 (12) (2011) 1619–1626. doi:10.1016/j.ress.2011.09.003.

[67] A. Hansen, S. Roux, Statistics Toolbox for Damage and Fracture, in: D. Krajcinovic, J. Van Mier (Eds.), Damage and Fracture of Disordered Materials, International Centre for Mechanical Sciences, Springer, Vienna, 2000, pp. 17–101. doi:10.1007/978-3-7091-2504-5_2.

[68] K. M. Salerno, M. O. Robbins, Effect of inertia on sheared disordered solids: Critical scaling of avalanches in two and three dimensions, Physical Review E 88 (6) (2013) 062206. doi:10.1103/PhysRevE.88.062206.

[69] F. Shimizu, S. Ogata, J. Li, Theory of Shear Banding in Metallic Glasses and Molecular Dynamics Calculations, Materials Transactions 48 (11) (2007) 2923–2927. doi:10.2320/matertrans.MJ200769.

[70] A. Stukowski, Visualization and analysis of atomistic simulation data with OVITO–the Open Visualization Tool, Modelling and Simulation in Materials Science and Engineering 18 (1) (2010) 015012. doi:10.1088/0965-0393/18/1/015012.

[71] C. C. Paige, M. A. Saunders, LSQR: An Algorithm for Sparse Linear Equations and Sparse Least Squares, ACM Transactions on Mathematical Software 8 (1) (1982) 43–71. doi:10.1145/355984.355989.